The International Journal of Advanced Manufacturing Technology (2019) 100:3045–3054
https://doi.org/10.1007/s00170-018-2899-4

ORIGINAL ARTICLE

The effects of collector geometry on the internal structure of the 3D nanofiber scaffold fabricated by divergent electrospinning

Yingge Zhou[1] · Zhiyong Hu[1] · Dongping Du[1] · George Z. Tan[1]

Received: 17 June 2018 / Accepted: 17 October 2018 / Published online: 24 October 2018

Abstract
Latest bioinspired approaches in tissue engineering focus on the creation of biomaterials with micro- and nanoscale topographical features. Various additive manufacturing techniques have been applied for scaffold fabrication; however, creating three dimensional (3D) nanofiber structure within a scaffold remains to be challenging. This paper presented an innovative divergence electrospinning strategy to fabricate 3D polycaprolactone (PCL) scaffolds comprised of uniaxially aligned nanofibers. The effects of collector geometry on the nanofiber structure were characterized by polynomial regression analysis. The length-to-width ratio and inclination angle of the collector were found to be critical to nanofiber distribution within the 3D scaffold. The nanofiber orientation was consistent with the direction of electric field vectors between the two bevels of the collector. After a continuous culturing for 7 days, fibroblast cells were uniaxially organized within the 3D scaffolds, closely resembling the fibrous structure in musculoskeletal tissues. This study provided a novel approach to biomimetic native tissue microstructures and showed a great potential as a future fabrication additive manufacturing platform for tissue engineering.

Keywords Divergence electrospinning · 3D nanofiber scaffold · Tissue engineering · Dimensional design

1 Introduction

Tissue engineering, together with materials science, bioengineering, and advanced manufacturing, has emerged as a research frontier and potential therapy for repair of living tissues using biomaterials, cells, and growth factors. To mimic the native tissue architecture, composites are engineered using organized scaffolds, a cellular solid support structure comprising an interconnected pore network or matrix to perform various functions, including the support of cell colonization, migration, growth and differentiation, and the formation of the extracellular matrix (ECM) [23]. Successful scaffolds should meet some basic requirements, generally involving biocompatibility, biodegradability with controlled kinetics, an interconnected porous structure with a tailored pore size, mechanical properties close to the target tissue and predefined geometry and size [25]. As net-shaping processes, additive manufacturing (AM) techniques offer a great potential to fabricate scaffolds for tissue engineering. A variety of AM techniques and methodologies have been studied to generate scaffolds with geometrically complex internal architecture. Common methods include fused deposition modeling (FDM) [11], stereolithography [8], inkjet printing [44], bioplotting technique [3, 27], direct laser writing [35] and selective laser sintering [22]. Although substantial progress has been made in AM for tissue engineering constructs in recent years, the resolution limits of most current AM processes are still at levels of sub-millimeter to 10 μm [6, 37]. Latest bioinspired approaches focus on the creation of biomaterials with micro- and nanoscale topographical features, macroscale gradient structures, and biological domains to interact with target growth factors and cells [31]. Nanotopography and local environment influence trends in cell behavior by providing chemical and physical stimuli to promote cell adhesion, proliferation, morphogenesis, and motility [24]. The dimension constraints limit the further applications of existing AM techniques to mimic the unique structures and properties of natural tissues.

Among various nanostructures, electrospun nanofibers have been extensively studied for scaffold applications [13, 47]. The ultra-thin continuous fibers can form non-woven webs which possess multiple desirable properties, such as

✉ George Z. Tan
george.z.tan@ttu.edu

[1] Department of Industrial Manufacturing & Systems Engineering, Texas Tech University, Lubbock, TX 79409, USA

high surface-to-volume ratio, highly interconnected porous structure, and adjustable pore size distribution, etc. The nanofibrous scaffolds mimic the ECM structure and provide an appropriate substrate for cell attachment and nutrient transport [2]. Various electrospinning strategies have been developed in recent decades. For example, Pan et al. obtained continuous and well-aligned fibers with two-needle electrospinning design, and it can be deposited over a large area [30]. With side-by-side electrospinning, Niu et al. fabricated interbonded nanofiber membranes with improved chemical and physical properties [28]. Shin et al. successfully incorporated sustainable released drug inside of nanofibers, with core-shell electrospinning design [36]. Other electrospinning strategies, such as magnetic electrospinning [43] and electrospinning with salt/polymer leaching [34], provide controllable, highly porous scaffolds as well.

One of the major disadvantages of conventional electrospun nanofibrous scaffolds, however, is the limited thickness (< 1 mm) attributed to the nature of electrospinning [5, 29]. Although 2D scaffolds were widely used in tissue engineering applications such as skin regeneration, for more complex tissues, they fail to reflect some fundamental and crucial aspects of in vivo environments, including cell communication in spatial context, mechanical cues, and nutrient transportation [33]. Compared with 2D scaffolds structure, 3D scaffolds have shown a superior performance in inducing cell differentiation and development [20], and genetic materials expression including ECM secretion and cell metabolism [12, 18]. Some efforts have been made to construct 3D nanofiber structures by post-processing the electrospun mats [10] or integrating electrospinning with other AM techniques [14, 17]; however, so far, few works have been reported in direct electrospinning of 3D scaffolds with nanofiber structure.

In this paper, we presented a novel electrospinning-based additive manufacturing technique for 3D scaffold comprised of polycaprolactone (PCL) nanofibers. This technique adopts customized collectors with two axisymmetric bevels to form a divergence electric field, which will induce a construction of uniaxially aligned nanofibers in a layer-by-layer manner [48]. Polycaprolactone (PCL) is one of the most popular synthetic materials for tissue engineering due to its excellent balance in biocompatibility, biodegradability, and mechanical properties. Preliminary study has demonstrated the feasibility of fabricating 3D nanofibrous scaffold by divergence electrospinning. The hypothesis of this study is that the variation of the electric field distribution will induce changes in the static electric field during electrospinning, thus influence the internal structure of the nanofiber scaffold. The objective of this study is to test this hypothesis by investigating the effects of the collector dimensional design on the gradients of nanofiber density and alignment.

2 Materials and methods

2.1 Polymer solution preparation

PCL (MW = 80,000) pellets, acetone (>= 99.5%), and N,N-Dimethylformamide (DMF, 99.8%) were purchased from Sigma-Aldrich® (St. Louis, MO, USA). Through preliminary experiments, we found that 15% (*w*/*w*) PCL polymer solution resulted in the highest-quality nanofibers. The PCL solution was prepared by dissolving PCL in DMF and acetone (1:1) through magnetic stirring for 4 h at room temperature. The viscosity of the PCL solution was measured by ALPHA SERIES Rotational Viscometer from Fungilab® (NY, USA).

2.2 Collector design

In the phase-1 study, the electric field distribution was changed by the width-to-height ratio of the double-bevel collector. We focused on the variation of electric field density in the horizontal direction. The designs of the double-bevel collectors were illustrated in Fig. 1. Two axisymmetric bevels formed a 115°-angle relative to the horizontal plane. Polylactic acid (PLA) collectors were 3D printed by Ultimaker 3 system (Ultimaker®, Cambridge, MA, USA). The inner surfaces of the two bevels were covered with aluminum foils which were grounded through wire connectors. The lengths of the collectors were set to be 50 mm, 25 mm, and 10 mm, resulting in three levels of length-to-width ratios, namely 1, 0.5, and 0.2.

In the phase-2 study, more factors were introduced to change the electric field distribution in all three axes (x-y-z). The variations in width, height, and inclination degree were analyzed. Each factor has two levels, resulting in a total of eight collectors. The dimensions of the eight collectors are summarized in Table 1.

2.3 Electrospinning process

The electrospinning process was performed on the TL-Pro-BM Robotic Electrospinning Platform (Tongli® Tech, China), with a 50-kV high voltage power source. The collectors were placed on a hollow insulating stand in the electrospinning chamber. The aluminum foils on collectors were grounded separately using electrical wires passing through the inner cavity of the stand (Fig. 1a). The electrospinning spinneret was placed at the central line of the collector. The double-bevel induced a divergent electric field so that nanofibers were deposited onto both bevels of the collector while formed connecting fibers in between. The process parameters were summarized in Table 2. Conventional electrospinning was performed by using a flat aluminum sheet as the collector to generate 2D random nanofiber mats.

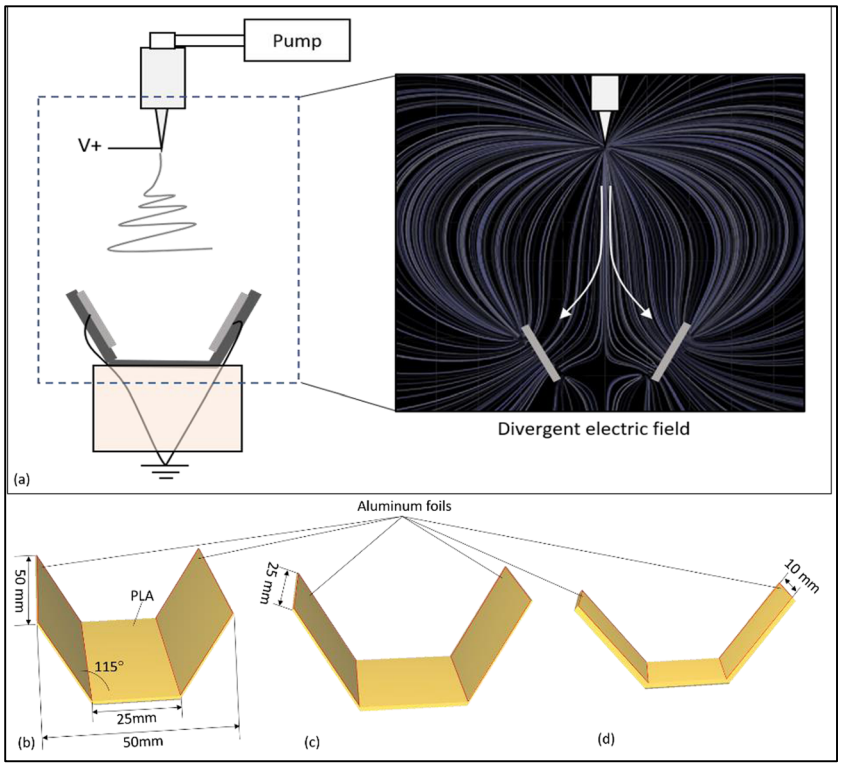

Fig. 1 **a** Electrospinning set up; Illustration of collectors with **b** 50-mm length, **c** 25-mm length, and **d** 10-mm length

2.4 Modeling of the static electric field

The static electric field of the divergence electrospinning was modeled and simulated by FlexPDE (PDE Solutions Inc., WA). The collector in Fig. 1b was employed for the simulation. A three-dimensional box was built to represent the electrospinning chamber, with the outer surfaces simulated as insulating surfaces (zero gradient in the potential). The collector without aluminum foil was modeled as an insulator as well. The conductivity of the steel nozzle and the aluminum foils was set to be 8.96×10^3 Siemens/mm and 3.54×10^4 Siemens/mm, respectively. The thickness of aluminum foil was 2 mm. The geometry of the nozzle was simplified to be a small cylinder with a radius of 2 mm and a length of 10 mm. Other parameters were set as the same as the actual experimental parameters.

Table 1 Dimensions for eight collectors

Collector code	Width (W)(mm)	Height (H)(mm)	Inclination degree (A)(°)
20w5h135a	20	5	135
20w5h120a	20	5	120
20w10h135a	20	10	135
20w10h120a	20	10	120
40w5h135a	40	5	135
40w5h120a	40	5	120
40w10h135a	40	10	135
40w10h120a	40	10	120

2.5 Scaffold characterization

Thin layers of nanofibers from the outer and inner sections of the electrospun scaffolds were collected using glass slides as illustrated in Fig. 2. Glass slides with double tapes were vertically inserted into each collector with equidistant gaps and swiped horizontally to collect nanofiber samples. In phase-1, two slides were used to collect each half of the nanofiber scaffold, while in phase-2, four slides were used to collect each quarter section of the scaffold. The nanofiber morphology and diameter were examined by scanning electron microscopy (SEM, Hitachi S-4300). The fiber density and alignment were characterized based on optical microscopy (Invitrogen™ AMF4300). For each glass slide, a series of optical microscope images with a scope of 1.1 mm were taken seamlessly to cover the full range of the collected nanofibers.

Table 2 Divergence electrospinning process parameters

Process parameters	Values
Pump rate	1.08 mL/h
Voltage	10 kV
Tip-to-base distance	100 mm
Nozzle size	22-gauge needle
Electrospinning time	2 min

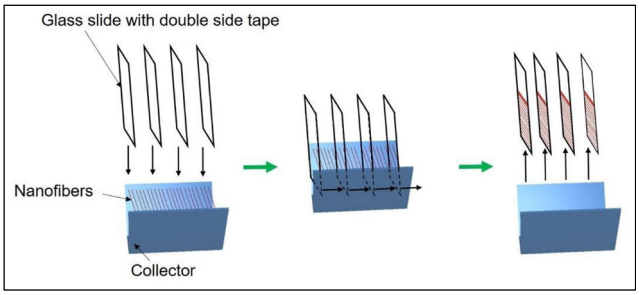

Fig. 2 Collection of nanofibers for quantitative studies

Fiber diameter was analyzed by DiameterJ (1.48) after the SEM images were segmented and processed. Fiber density was characterized by counting the number of fibers that intersected with a middle line across a binary SEM image. To quantify the fiber alignment, a fiber orientation histogram was created by ImageJ (1.8) for each image. The percentage of fibers within the 20-degree range around the peak value was calculated. A higher percentage represented a higher degree of fiber alignment. All Data were plotted by MATLAB into 3D graphs. The gradient of the nanofiber attribute within one scaffold was calculated by:

$$\text{Grad} = \left(1 - \frac{\text{Min(data point cloud)}}{\text{Max(data point cloud)}}\right) \times 100\%$$

2.6 Cell culture study

The 3D nanofiber scaffolds for cell culture study were fabricated by a scaled collector (width 20 mm, height 10 mm, inclination angle 135°) to fit the 6-well tissue culture plate. 2D random nanofiber mats (23 mm × 23 mm) served as the control group. Human fibroblasts (ATCC® MRC-5) were seeded on the scaffolds with an initial concentration of 200 k cells/ml in Eagles's Minimum Essential Medium (EMEM, ATCC®, Manassas, VA) with 10% fetal bovine serum (ATCC®, Manassas, VA). The collectors were sterilized with 72% ethanol before electrospinning and the scaffolds were UV-sterilized for 30 min after electrospinning. The scaffolds were incubated at 37 °C overnight for cells to attach and then transferred to new tissue culture wells for continuous culturing until the cell confluency reached approximately 80%. Finally, the cells were fixed with 4% formaldehyde, and stained with Phalloidin Phalloidin CruzFluor™ 488 Conjugate (Santa Cruz Biotechnology, Dallas, TX) and 4′,6-diamidino-2-phenylindole (DAPI, Santa Cruz Biotechnology, Dallas, TX) for filamentous F-actin and nucleus, respectively.

3 Results

The viscosity of the 15% PCL solution was approximately 1330 mPa s. At this viscosity, fine electrospun nanofibers were obtained without beads. In phase-1, nanofibers formed mats on the surfaces of two bevels and an aligned web structure between the two bevels from bottom to top (Fig. 3). However, for the 10-mm collector, the nanofiber started agglomerating at the top of the collector after 1 min and formed twisted bundles between the spinneret and the top edge of the collector. The bundles were manually removed after the electrospinning. It was observed that the fiber density was higher at the top layers than at the bottom layers for all three collectors. The 25-mm collector had the densest fibers on the side and top of the collector. SEM images of the nanofibers were presented in Fig. 4. All double-bevel collectors resulted in a highly aligned fiber organization, compared to the random fiber distribution obtained by the conventional 2D electrospinning configuration. The scaffold in the 25-mm collector showed the highest fiber density among the three designs.

A summary of fiber diameter distribution was shown in Fig. 5**a**. All the electrospun fibers were at nanoscale, ranging from 154 nm to 621 nm. The mean diameter of the nanofibers was between 468 and 314 nm. No substantial difference in fiber diameter was found among different scaffolds or between 3D nanofibers and 2D nanofibers.

A quantitative analysis of fiber density was summarized in Fig. 5b**.** The mean fiber densities of the 3D scaffolds were 1–2 orders of magnitude lower than that of 2D mat. Therefore the porosity of the 3D scaffolds was much higher than that of 2D mat. A gradient in fiber density along the z-axis of the collector was confirmed for all three designs. The 25-mm collector saw the densest fibers on both top layer and bottom layer among the three collectors, while the 50-mm collector had the lowest fiber density. The gradient degree, namely the ratio of fiber density at the top layer to that at the bottom layer, also varied among three collectors. It was obvious that the effect of collector geometry had a non-linear effect on the nanofiber

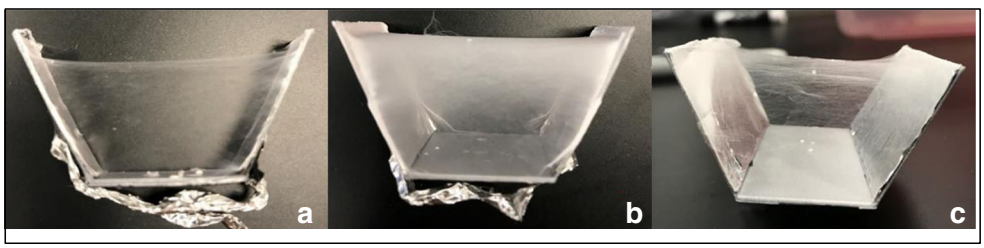

Fig. 3 Electrospun nanofiber scaffolds obtained by **a** 10-mm collector, **b** 25-mm collector, and **c** 50-mm collector

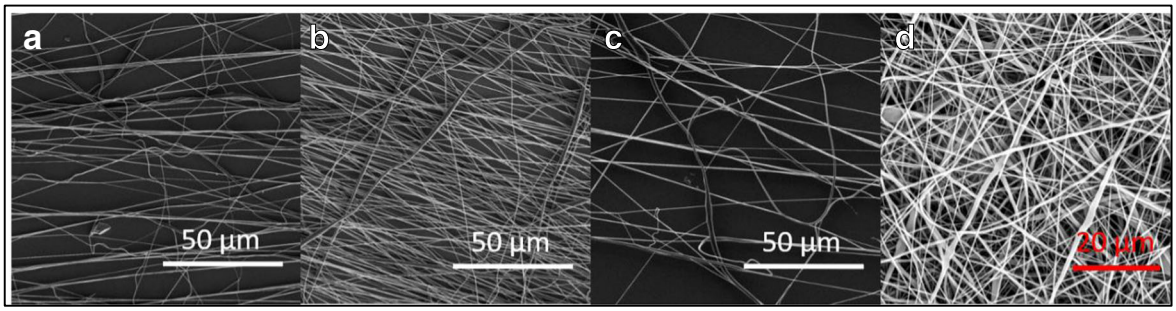

Fig. 4 SEM images of nanofibers from **a**, **b**, **c** the top layer of 10-mm, 25-mm, and 50-mm collectors, and **d** electrospun 2D mat

distribution. The 25-mm collector had the greatest gradient, while the 10-mm collector and 50-mm collector had the equivalent gradient. The non-linear relationships between the collector geometry and fiber density were approximated by polynomial regression lines given as below with high goodness-of-fit ($R^2 \approx 1$):

$$y = -117.75x^2 + 465.25x - 299.25 \text{ (Top layer)} \quad (1)$$

$$y = -4.875x^2 + 16.625x - 0.25 \text{ (Bottom layer)} \quad (2)$$

where y is fiber density in 100 × 100 μm area and x the length-to-width ratio of the double-bevel collector.

The 25-mm collector resulted in the highest fiber density gradient, while the 10-mm collector had the lowest gradient. The polynomial regression line was given as

$$z = -6.5769x^2 + 27.405x - 16.633 \quad (3)$$

where z is fiber density ratio.

In the phase-2 study, three factors were studied, namely width, height, and inclination angle, so that the electric field was altered in three dimensions. The fiber density gradients for all eight configurations were summarized in Fig. 6. In the MATLAB plots, height represents the vertical direction of the collector, and section represents the horizontal direction. The gradient in fiber density decreased with a larger inclination angle. For example, the fiber density gradient of the scaffold in the 40W10H135A collector was 84.7%, which was approximately 15% lower than that in the 40W10H120A collector. The 40W5H135A collector resulted in a fiber density gradient of 72.5%, compared to 83.4% from the 40W5H120A. The results showed that when the collector the inclination angle increased, more fibers were obtained at the lower section of the collector. The collector height also seemed to be positively correlated to the fiber density gradient. As height increased, the differences in fiber density between the top section and the lower section of the scaffold also increased. However, this was largely due to the difference in scaffold thickness. Within the same thickness range, the effect of collector height was negligible.

The fiber alignment gradients for all eight collectors were summarized in Fig. 7. Collector height and width did not show significant effect on the fiber alignment gradient. However, inclination angle had a negative effect on fiber alignment gradient. For example, the fiber alignment gradient of the scaffold in the 40W10H135A collector was 26.7%, while that of the scaffold in the 40W10H120A collector was increased to 57.2%. Similarly, the fiber alignment gradients in the 40W5H135A collector and the 40W5H120A collector were 34.5% and 43.9%, respectively. The average alignment level increased from 42.98% to 56.32% with inclination angle increases from 120° to 135°. High inclination angle resulted in more uniform nanofiber organization.

The front-view potential profile of the divergence electrospinning was displayed in Fig. 8a. Within the collector,

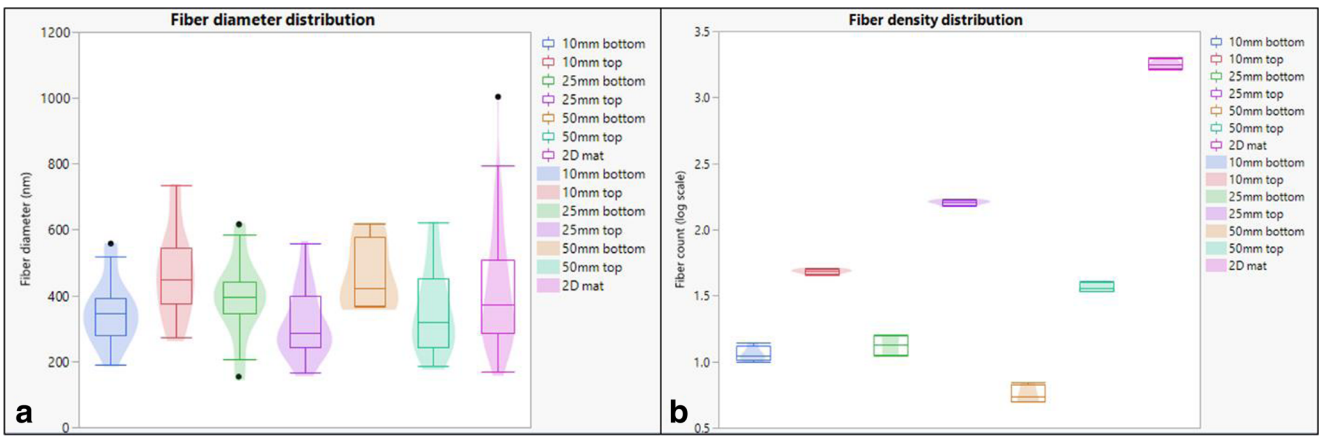

Fig. 5 Violin/box plots for **a** fiber diameter distribution, and **b** fiber density distribution

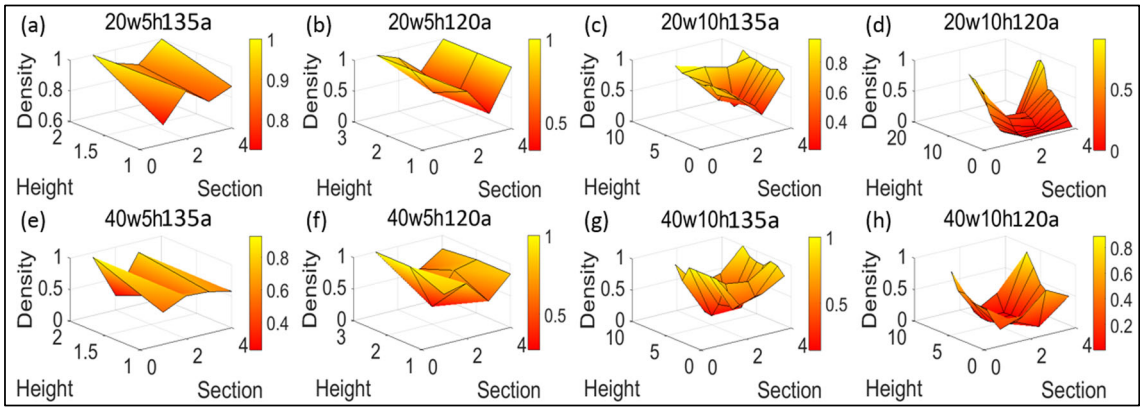

Fig. 6 Fiber density plots for eight collectors

there is little change in electric potential along the z-axis. The contour plots of the electric field vectors were shown in Fig. 8b. The field is axially symmetric and diverges at the top surface of the collector. The cross-section potential profiles at selected planes from top to bottom were shown in Fig. 8c–f. It is clear that the 2D potential profile gradually changes from a circle to an ellipse and finally merges into two parallel lines as it moves from the electrospinning tip to the collector.

The fluorescent cell culture images were shown in Fig. 9. For the 3D scaffold comprised of aligned nanofibers (Fig. 9a), fibroblasts were stretched along the fiber orientation. The nanofibers maintained a bundle structure in the culture medium and provided enough mechanical support for cells to attach and proliferate. In addition, the peripheral areas of the picture were out of focus showing that the cells were distributed in a 3D space. For the 2D mat comprised of random nanofibers (Fig. 9b), cells were randomly distributed on a flat surface. The low porosity impeded the infiltration of cells into the mat.

4 Discussion

Because the structure of natural extracellular matrices varies substantially for different tissues, there has been a growing awareness that the hierarchical 3D structure of scaffolds may affect the intercellular interactions, the material transportation, fluid flow, environmental stimulation etc., and further influence the tissue growth and formation. Therefore, there is a growing research need for the development of biomimical scaffolds with intrinsic biological and microstructural properties. The scaffold developed in this study can be directly embedded in cell-laden hydrogel to form the aligned nanofiber support and guidance for cell proliferation in 3D structure. This technique can be applied in the engineering of musculoskeletal soft tissues such as tendons, ligaments, knee menisci, etc.[13], where a fibrous cytoskeletal organization is critical for tissue formation and functions.

One of the most common methods for 3D organization of the nanofibers is to process the nanofibrous mesh into desirable form after the electrospinning. For example, a 3D scaffold can be created by stacking multiple layers of nanofiber mesh for cell seeding [19, 32, 45]. An aligned nanofiber mesh can also be rolled onto a tubular [41] or core-shell structure [40]. The advantage of this method is the high degree of flexibility in creating the final form of scaffolds. Concurrent nanofiber mesh formation can be achieved by utilizing intermediate supporting substrate, in either liquid or solid form, to collect nanofibers. Water and solvents such as methanol and

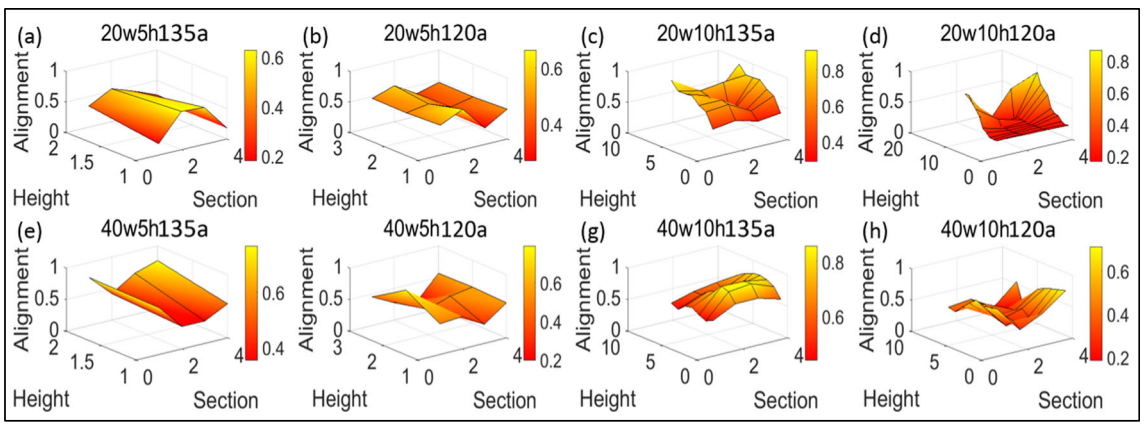

Fig. 7 Fiber alignment plots for eight collectors

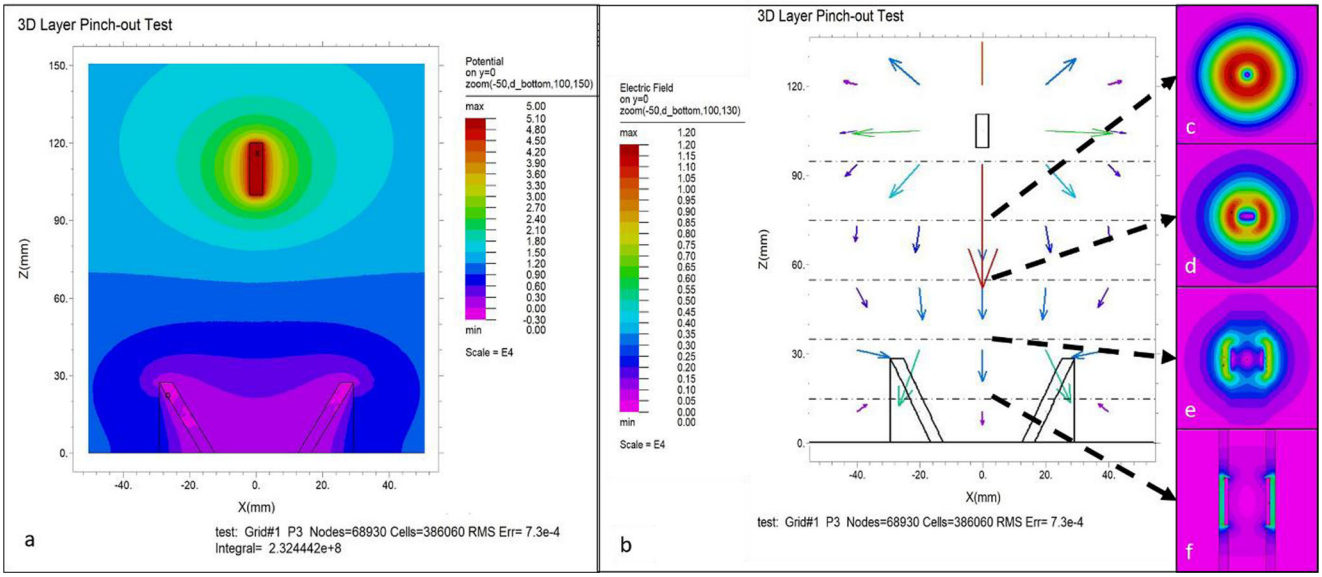

Fig. 8 Simulated electric field distribution of the divergence electrospinning. **a** Equal potential profile from the front view. **b** Electric field density vectors from the front view. **c** Equal potential profile from the top view at 75 mm. **d** Equal potential profile from the top view at at 55 mm. **e** Equal potential profile from the top view at 35 mm. **f** Equal potential profile from the top view at 15 mm

ethanol have been used as the liquid collector due to their low surface tension, which allows easy assembly of the deposited mesh into a yarn [9, 46] or a 3D nanofibrous scaffold [15] without breaking the fibers. To overcome the compaction of the deposited fibers, salt particles [26] or sacrificial polymers [1] can be sprinkled concurrently with electrospinning. These additives enable rapid build-up of the nanofibrous volume and can be washed away after the desired thickness is reached. A more effective method is to neutralize the deposited mash during the electrospinning by a charged electrode so that the nanofiber may decelerate sufficiently and a charged air current may be used to gather the nanofibers into block structures [4, 39]. Electrospinning can also be integrated into a hybrid manufacturing process which creates scaffolds with microfiber decks and nanofiber fillers. This process may require rapid prototyping technique [21, 38] to build the body of scaffolds, or different settings of electrospinning to create different layers of fibers [16].

The divergence electrospinning strategy presented in this paper was able to directly fabricate nanofiber scaffold with spatial structures in a bottom-up manner. The nanofibers were uniaxially aligned in the 3D scaffold. The results from fiber density analysis revealed a gradient of fiber density from top to bottom layers: all the collectors showed a significant decrease in fiber density from top to bottom. A majority of the nanofibers were accumulated at the peripheral area of the collector. We hypothesized that this phenomenon was due to the repulsive effects attributed to the residual charges on the electrospun nanofibers. For regular electrospinning, the nanofibers are deposited on a grounded surface, where the repulsive forces from the accumulated residual charges are fractional compared to the static electric force until the fiber density and thickness reach a very high level. In our case, the bridging nanofibers were hanged between two grounded bevels. The static electric forces exerted on the nanofiber were diverged to two directions, led to a weaker resultant force downward.

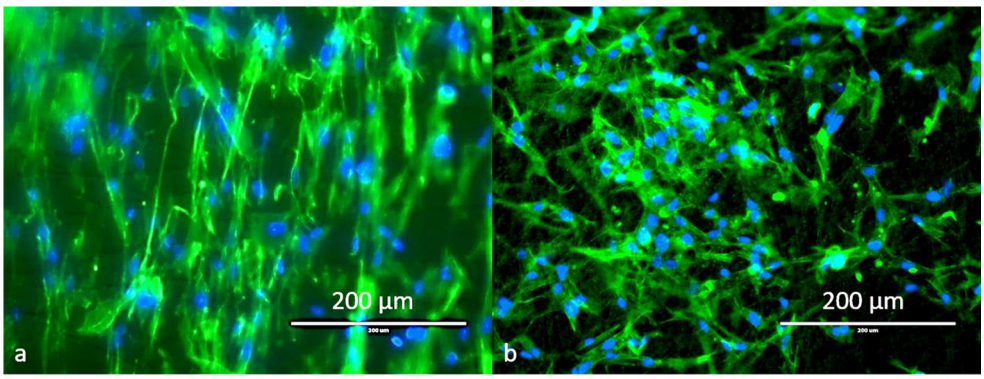

Fig. 9 Florescent images for cells in **a** a 3D scaffold and **b** a 2D mat. The nuclei were stained blue and the filamentous actins were stained green

When nanofibers accumulated, the repulsive forces between the fibers might soon exceed the static electric forces and thus pushed the later electrospun fibers to the peripheral space. Once the nanofibers at the peripheral areas became denser, it would be more difficult for the electrospun jet reach the central area. Therefore, the gradient of fiber density would only increase as electrospinning continued.

It was found that the geometry of the double-bevel collector, specifically the length-to-width ratio and the inclination angle, influenced the nanofiber distribution within the 3D scaffold. These factors essentially influenced the structure of static electric field between the spinneret and the grounded aluminum foils which acted as two electrodes. The 10-mm collector showed the lowest fiber density gradient; however, it resulted in an undesired agglomerate fiber bundle on the top layer, which was not included in the fiber density analysis. With a lower length-to-width ratio, the static electric field could be highly distorted near the collector, inducing unstable nanofiber trajectory which prevented fiber bridging between the two bevels. The 25-mm collector had the highest fiber density at both top and bottom layers, indicating that a balanced static field is critical to sustaining a stable fiber bridging effect between the two axisymmetric bevels. In addition, the 50 mm collector showed the lowest fiber density inside the collector, which is probably attributed to its highest space volume. With the same amount of polymer solution, the nanofiber density will be lower in a larger space. The results indicated that there should be an optimal range of the length-to-width ratio of the collector to fabricate a 3D nanofiber scaffold with a maximized fiber density and a homogenous fiber distribution. Furthermore, the inclination angle substantially influenced the microstructure homogeneity of the nanofiber scaffold. The polarization of nanofiber density and alignment can be significantly reduced by adopting a high inclination angle. This phenomenon is probably due to the change of intensity gradient of the electric field towards the inner surfaces of the collector bevels. The electric field gradient decreases as the inclination angle increases, which can mitigate the instability of the nanofiber self-assembly.

With regard to nanofiber diameter, the collector geometry did not show a significant influence. Fridrikh et al. [7] proposed an analytical model for the forces that determine jet diameter during electrospinning. The model solves the equations of motion for the jet, as a function of material properties [dielectric permittivity ($\bar{\varepsilon}$), surface tension (γ)] as well as operating characteristics [flow rate (Q), electric current (I)]

$$h_t = \left(\gamma\bar{\varepsilon}\frac{Q^2}{I^2}\ \frac{2}{\pi(2ln\chi-3)}\right)^{\frac{1}{3}} \tag{4}$$

where h_t is the terminal jet diameter, χ=R/h is the dimensionless wavelength of the bending instability (R is the radius of the bending perturbation and h is the jet radius). Equation (4) predicts that the terminal diameter of the whipping jet is controlled by the flow rate, electric current, and the surface tension of the fluid. Equation (4) neglects elastic effects and fluid evaporation, and also assumes minimal jet thinning after the saturation of the whipping instability. They also found that theoretical predictions were in agreement with experimental data obtained from electrospinning PCL solutions.

Thompson et al. [42] established a theoretical model to characterize the effects of material and operating parameters on electrospun fiber diameters. The results show that the five parameters (volumetric charge density, distance from nozzle to the collector, initial jet/orifice radius, relaxation time, and viscosity) have the most significant effect on the jet radius. The governing quasi-one-dimensional continuity, momentum and charge conservation equations were given as follows:

$$\frac{\partial\lambda f}{\partial t} = -j_{ev} \tag{5}$$

$$\rho\frac{\partial\lambda fV}{\partial t} = \tau\frac{\partial P}{\partial t} + \lambda|k|Pn + \lambda|k|(\pi a\sigma - q_{e1})n - \lambda e\frac{U_0}{h}k \tag{6}$$

$$e\lambda = e_0\lambda_0 \tag{7}$$

where λ is geometrical In Eq. (4) l is the geometrical stretching ratio, $f=\pi a^2$ is the cross-sectional area (a: the cross-sectional radius), subscript zero denotes the parameter values at time $t=0$. ρ is the liquid density, V is velocity vector, P is the longitudinal force in the jet cross-section, U_0/h is the outer electric field strength (U_0: the potential difference, h: the inter-electrode distance), σ is the surface tension, k is the local curvature of the jet axis, e is the charge per unit jet length, $q_{e1}$is the net Coulomb force acting on a jet element, and j_{ev} is the flux describing mass loss due to solvent evaporation. In Eq. (6), the inter-electrode distance h (distance between nozzle and collector) has a negative relationship with cross-sectional fiber diameter. Given that the height of the collectors in this study was marginal relative to the jet travel distance, no substantial change in fiber diameter was found.

The modeling of the electric field revealed that the nanofiber orientation was consistent with the direction of electric field vectors between the two bevels of the collector. Because the two bevels were symmetric to the electrospinning tip, the top-view potential profile of the collector can be simplified as two parallel rectangles with equal field strength gradient, which caused the whipping polymer jets to form a highly aligned nanofiber matrix. The change of collector geometry, such as height and angle, will influence the field strength gradient along z-axis, thus may affect the nanofiber organization. The simulation also showed that there was no gradient of the field strength within the collector. Therefore, we speculate that the nanofiber density gradient was due to the charge retention of the deposited nanofibers. PCL, like many other polymers, is poor electrical conductor therefore tends to retain charges after electrospinning. The repulsive forces among

charged nanofibers decentralized the fiber deposition, resulting in a higher fiber density at the peripheral areas of the scaffold.

In the fluorescent cell culture images, we observed that in the 3D nanofiber scaffold, the cells were uniaxially organized within the whole space, closely resembling the common fibrous structure in musculoskeletal tissues. This is the main advantage over conventional 2D nanofiber scaffold in which cells were randomly distributed only on the surface. We believe that the 3D nanofiber scaffold with a biomimetic pattern provides a novel solution for creating the microarchitecture of extracellular matrix on a clinically relevant scale. It should be noted that most of the fibroblasts were accumulated on the peripheral areas of the 3D scaffold, and the cell density was positively correlated to the nanofiber density. The homogeneity of nanofiber distribution needs to be enhanced in future work.

Future work will focus on homogenization of the fiber density within the 3D scaffold by minimizing the residual charges on the fibers. Potential methods include an increase of the polymer concentration, addition of inorganic salts in solution, etc. In addition, mechanism-based models will be needed to describe, simulate, and predict the divergence electrospinning process to optimize the outcomes.

5 Conclusion

This paper presented a novel divergence electrospinning strategy with double-bevel collectors for 3D nanofiber scaffold fabrication. The effects of electric field distribution on fiber density and diameter were characterized. The results showed that the geometry of the double-bevel collector, specifically the length-to-width ratio and the inclination angle, influenced the nanofiber organization within the 3D scaffold. A length-to-width ratio close to one and a high inclination angle are desirable to achieve more homogenous nanofibrous structure. This study provided an innovative approach to biomimic native tissue microstructures and showed a great potential as a future fabrication AM platform for tissue engineering.

Funding information This work was financially supported by the Foundation of the Whitacre College of Engineering and the Office of Vice President for Research at Texas Tech University.

References

1. Baker BM, Gee AO, Metter RB, Nathan AS, Marklein RA, Burdick JA, Mauck RL (2008) The potential to improve cell infiltration in composite fiber-aligned electrospun scaffolds by the selective removal of sacrificial fibers. Biomaterials 29(15):2348–2358
2. Bettinger CJ, Langer R, Borenstein JT (2009) Engineering substrate topography at the micro-and nanoscale to control cell function. Angew Chem Int Ed 48(30):5406–5415
3. Billiet T, Gevaert E, De Schryver T, Cornelissen M, Dubruel P (2014) The 3D printing of gelatin methacrylamide cell-laden tissue-engineered constructs with high cell viability. Biomaterials 35(1):49–62
4. Bonino CA, Efimenko K, Jeong SI, Krebs MD, Alsberg E, Khan SA (2012) Three-dimensional electrospun alginate nanofiber mats via tailored charge repulsions. Small 8(12):1928–1936
5. Fisher MB, Henning EA, Söegaard N, Esterhai JL, Mauck RL (2013) Organized nanofibrous scaffolds that mimic the macroscopic and microscopic architecture of the knee meniscus. Acta Biomater 9(1):4496–4504
6. Fricain J-C, De Olivera H, Devillard R, Kalisky J, Remy M, Keriquel V et al (2017) 3D bioprinting in regenerative medicine and tissue engineering. *Medecine* sciences*: M/S* 33(1):52–59
7. Fridrikh SV, Jian HY, Brenner MP, Rutledge GC (2003) Controlling the fiber diameter during electrospinning. Phys Rev Lett 90(14): 144502
8. Gauvin R, Chen Y-C, Lee JW, Soman P, Zorlutuna P, Nichol JW et al (2012) Microfabrication of complex porous tissue engineering scaffolds using 3D projection stereolithography. Biomaterials 33(15):3824–3834
9. Hashizume R, Fujimoto KL, Hong Y, Amoroso NJ, Tobita K, Miki T et al (2010) Morphological and mechanical characteristics of the reconstructed rat abdominal wall following use of a wet electrospun biodegradable polyurethane elastomer scaffold. Biomaterials 31(12):3253–3265
10. He X, Feng B, Huang C, Wang H, Ge Y, Hu R et al (2015) Electrospun gelatin/polycaprolactone nanofibrous membranes combined with a coculture of bone marrow stromal cells and chondrocytes for cartilage engineering. Int J Nanomedicine 10: 2089
11. Hutmacher DW, Schantz T, Zein I, Ng KW, Teoh SH, Tan KC (2001) Mechanical properties and cell cultural response of polycaprolactone scaffolds designed and fabricated via fused deposition modeling. J Biomed Mater Res A 55(2):203–216
12. Hwang NS, Kim MS, Sampattavanich S, Baek JH, Zhang Z, Elisseeff J (2006) Effects of three-dimensional culture and growth factors on the chondrogenic differentiation of murine embryonic stem cells. Stem Cells 24(2):284–291
13. Jiang T, Carbone EJ, Lo KW-H, Laurencin CT (2015) Electrospinning of polymer nanofibers for tissue regeneration. Prog Polym Sci 46:1–24
14. Kang H-W, Lee SJ, Ko IK, Kengla C, Yoo JJ, Atala A (2016) A 3D bioprinting system to produce human-scale tissue constructs with structural integrity. Nat Biotechnol 34(3):312–319
15. Khil MS, Bhattarai SR, Kim HY, Kim SZ, Lee KH (2005) Novel fabricated matrix via electrospinning for tissue engineering. J Biomed Mater Res B Appl Biomater 72(1):117–124
16. Kim G, Son J, Park S, Kim W (2008) Hybrid process for fabricating 3D hierarchical scaffolds combining rapid prototyping and electrospinning. Macromol Rapid Commun 29(19):1577–1581
17. Lee S-J, Nowicki M, Harris B, Zhang LG (2017) Fabrication of a highly aligned neural scaffold via a table top stereolithography 3D printing and electrospinning. Tissue Eng A 23(11–12):491–502
18. Liu H, Lin J, Roy K (2006) Effect of 3D scaffold and dynamic culture condition on the global gene expression profile of mouse embryonic stem cells. Biomaterials 27(36):5978–5989
19. Madurantakam PA, Rodriguez IA, Garg K, McCool JM, Moon PC, Bowlin GL (2013) Compression of multilayered composite electrospun scaffolds: a novel strategy to rapidly enhance mechanical properties and three dimensionality of bone scaffolds. Adv Mater Sci Eng 2013:1–9

20. Malda J, Woodfield T, Van Der Vloodt F, Wilson C, Martens D, Tramper J et al (2005) The effect of PEGT/PBT scaffold architecture on the composition of tissue engineered cartilage. Biomaterials 26(1):63–72
21. Martins A, Chung S, Pedro AJ, Sousa RA, Marques AP, Reis RL, Neves NM (2009) Hierarchical starch-based fibrous scaffold for bone tissue engineering applications. J Tissue Eng Regen Med 3(1):37–42
22. Mazzoli A (2013) Selective laser sintering in biomedical engineering. Medical & biological engineering & computing 51(3):245–256
23. Melchels FP, Domingos MA, Klein TJ, Malda J, Bartolo PJ, Hutmacher DW (2012) Additive manufacturing of tissues and organs. Prog Polym Sci 37(8):1079–1104
24. Mendes PM (2013) Cellular nanotechnology: making biological interfaces smarter. Chem Soc Rev 42(24):9207–9218
25. Mota C, Puppi D, Chiellini F, Chiellini E (2015) Additive manufacturing techniques for the production of tissue engineering constructs. J Tissue Eng Regen Med 9(3):174–190
26. Nam J, Huang Y, Agarwal S, Lannutti J (2007) Improved cellular infiltration in electrospun fiber via engineered porosity. Tissue Eng 13(9):2249–2257
27. Narayanan LK, Huebner P, Fisher MB, Spang JT, Starly B, Shirwaiker RA (2016) 3D-bioprinting of polylactic acid (PLA) nanofiber–alginate hydrogel bioink containing human adipose-derived stem cells. ACS Biomaterials Science & Engineering 2(10):1732–1742
28. Niu H, Zhang J, Xie Z, Wang X, Lin T (2011) Preparation, structure and supercapacitance of bonded carbon nanofiber electrode materials. Carbon 49(7):2380–2388
29. Nowlin, J., Bismi, M. A., Delpech, B., Dumas, P., Zhou, Y., & Tan, G. Z. (2018). Engineering the hard–soft tissue interface with random-to-aligned nanofiber scaffolds. *Nanobiomedicine*
30. Pan H, Li L, Hu L, Cui X (2006) Continuous aligned polymer fibers produced by a modified electrospinning method. Polymer 47(14): 4901–4904
31. Peng S, Jin G, Li L, Li K, Srinivasan M, Ramakrishna S, Chen J (2016) Multi-functional electrospun nanofibres for advances in tissue regeneration, energy conversion & storage, and water treatment. Chem Soc Rev 45(5):1225–1241
32. Pham QP, Sharma U, Mikos AG (2006) Electrospun poly (ε-caprolactone) microfiber and multilayer nanofiber/microfiber scaffolds: characterization of scaffolds and measurement of cellular infiltration. Biomacromolecules 7(10):2796–2805
33. Rinker TE, Temenoff JS (2014) Micro-and nanotechnology engineering strategies for tissue interface regeneration and repair. In: Tissue and organ regeneration: advances in micro-and nanotechnology, p 105
34. Sakaguchi, H., Amoroso, N., & Wagner, W. (2014). Engineering electrospun scaffolds to encourage cell infiltration *Engineered Cell Manipulation for Biomedical Application* (pp. 75–94): Springer
35. Selimis A, Mironov V, Farsari M (2015) Direct laser writing: principles and materials for scaffold 3D printing. Microelectron Eng 132:83–89
36. Shin S-H, Purevdorj O, Castano O, Planell JA, Kim H-W (2012) A short review: recent advances in electrospinning for bone tissue regeneration. Journal of tissue engineering 3(1): 2041731412443530
37. Shirazi SFS, Gharehkhani S, Mehrali M, Yarmand H, Metselaar HSC, Kadri NA, Osman NAA (2015) A review on powder-based additive manufacturing for tissue engineering: selective laser sintering and inkjet 3D printing. Sci Technol Adv Mater 16(3): 033502
38. Silva NA, Salgado AJ, Sousa RA, Oliveira JT, Pedro AJ, Leite-Almeida H et al (2009) Development and characterization of a novel hybrid tissue engineering–based scaffold for spinal cord injury repair. Tissue Eng A 16(1):45–54
39. Sun B, Long Y-Z, Yu F, Li M-M, Zhang H-D, Li W-J, Xu T-X (2012) Self-assembly of a three-dimensional fibrous polymer sponge by electrospinning. Nanoscale 4(6):2134–2137
40. Sun Z, Zussman E, Yarin AL, Wendorff JH, Greiner A (2003) Compound core–shell polymer nanofibers by co-electrospinning. Adv Mater 15(22):1929–1932
41. Teo W, Kotaki M, Mo X, Ramakrishna S (2005) Porous tubular structures with controlled fibre orientation using a modified electrospinning method. Nanotechnology 16(6):918–924
42. Thompson C, Chase GG, Yarin A, Reneker D (2007) Effects of parameters on nanofiber diameter determined from electrospinning model. Polymer 48(23):6913–6922
43. Xu L, Wang L, Si N, He J (2013a) Aligned nanofibers by magnetic-electrospinning for biomedical applications. J Control Release 172(1):e131–e132
44. Xu T, Zhao W, Zhu J-M, Albanna MZ, Yoo JJ, Atala A (2013b) Complex heterogeneous tissue constructs containing multiple cell types prepared by inkjet printing technology. Biomaterials 34(1): 130–139
45. Yang X, Shah JD, Wang H (2008) Nanofiber enabled layer-by-layer approach toward three-dimensional tissue formation. Tissue Eng A 15(4):945–956
46. Yokoyama Y, Hattori S, Yoshikawa C, Yasuda Y, Koyama H, Takato T, Kobayashi H (2009) Novel wet electrospinning system for fabrication of spongiform nanofiber 3-dimensional fabric. Mater Lett 63(9):754–756
47. Zhou, Y., & Tan, G. Z. (2017). Fabrication of nanofiber mats with microstructure gradient by cone electrospinning. Nanomaterials and Nanotechnology, 7, 1847980417748478, 184798041774847
48. Zhou, Y., & Tan, G. Z. (2018). Generation of 3D nanofiber structure by divergence electrospinning for tissue engineering scaffold. Paper presented at the ASME 2018 13th International Manufacturing Science and Engineering Conference